Steel and Composite Structures, *Vol. 34, No. 6* (*2020*) *819-835*
DOI: https://doi.org/10.12989/scs.2020.34.6.819

Temperature variation in steel beams subjected to thermal loads

Sallal R. Abid*

Department of Civil Engineering, University of Wasit, Kut, Iraq

(*Received July 12, 2019, Revised December 12, 2019, Accepted February 13, 2020*)

Abstract. The effects of atmospheric thermal loads on the response of structural elements that are exposed to open environments have been recognized by research works and design specifications. The main source of atmospheric heat is solar radiation, which dominates the variation of the temperature of air, earth surface and all exposed objects. The temperature distribution along the depth of steel members may differ with the geometry configuration, which means that the different-configuration steel members may suffer different thermally induced strains and stresses. In this research, an experimental steel beam was instrumented with many thermocouples in addition to other sensors. Surface temperatures, air temperature, solar radiation and wind speed measurements were recorded continuously for 21 summer days. Based on a finite element thermal analysis, which was verified using the experimental records, several parametric studies were directed to investigate the effect of the geometrical parameters of AISC standard steel sections on their thermal response. The results showed that the overall size of the beam, its depth and the thickness of its elements are of significant effect on vertical temperature distributions and temperature differences.

Keywords: steel beam; environmental thermal loads; temperature; temperature difference; solar radiation

1. Introduction

During the construction of steel structures, most of the structure members are exposed to thermal loads induced from solar radiation and air temperature. These loads are time-dependent and vary during the single day and from one to another. Fig. 1 shows the different thermal load components that affect the beam surfaces. During the day hours (heating hours), sunrays either strike the surfaces directly where there are no obstructions that prevent the direct beam radiation, or absorbed by the cloud cover and sky pollutants and a fraction of which reaches the surfaces as diffuse radiation. On the other hand, a fraction of the solar radiation reaching the ground surface is reflected back to the nearby beams depending on the ground reflectivity as shown in Fig. 1. When a beam surface receives solar radiation it also reflects a fraction of which depending on its absorptivity. Thus, reflected radiations from other surfaces can also affect each surface that share mutual vision (surface-to-surface radiation). During the night hours, the contact with the cold surrounding air cools down the hot surface by means of thermal convection, which depends on the temperature and speed of air. On the other hand, and as the beam can be considered as a grey body, it reradiates back to the atmosphere the absorbed energy from solar radiation by means of long wave radiation. The two mentioned cooling processes balance back the temperature of steel beams to a datum that is close to air temperature before sunrise.

*Corresponding author, Professor
E-mail: sallal@uowasit.edu.iq

In practice, some parts of structures under construction or all of which are in some cases keep exposed to open environment for long periods due to many reasons. Among these reasons maybe the inaccurate design of work plan, work problems and management issues or accidents that delay the work continuity for specific periods, or construction deficiencies that require structural evaluation before work restarting. Large scale natural disasters can also postpone constructional projects for long times. In such cases, the structure would be subjected to unfavorable number of heating and cooling cycles due to the continuous exposure to the time-dependent fluctuation of thermal loads. The daily and seasonally variation of solar radiation and air temperature can induce thermal deformations or stresses that affect the structural response (Chen *et al*. 2018, Zhao *et al*. 2017, Gaussian 2009).

Many researches were conducted on the effects of environmental thermal loads on temperature distributions in concrete, steel and composite structures. The most focus was on bridge girders as they are continuously exposed to open environments. Some recent experimental studies (Kulprapha and Warnitchai 2012, Song *et al*. 2012, Kromanis and Kripakaran 2014, Nandan and Singh 2014, Abid *et al*. 2016a, Abid *et al*. 2017, Numan *et al*. 2016) attempted to evaluate the effect of thermal loads on beams and girders. However, the available literature on steel structures is limited compared to concrete structures.

Based on the extreme value analysis, Lucas *et al.* (2003) used a three-year temperature data from sensors installed on a steel box girder bridge to evaluate the thermal actions of thermal loads for a long return period. Kim *et al.* (2015) numerically investigated the effect of solar radiation on a steel box girder of a cable-style bridge during the

ISSN: 1229-9367 (Print), 1598-6233 (Online)

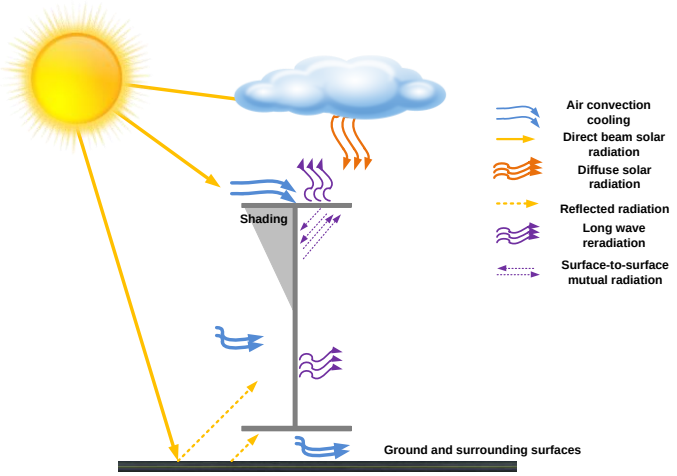

Fig. 1 Environmental thermal loads on the steel beam

construction period based on measured temperature data. The different temperature variations in flanges and webs were discussed. Alinia and Kashizadeh (2006a, b) investigated the thermal response of a space truss dome. In their studies, the effect of different uniform temperature changes and temperature gradients on deformations and stresses were investigated. Liu *et al*. (2013a, b) numerically investigated the thermal response and temperature distributions in large span steel structures with box-section members. The finite element model was verified using experimental measurements on a steel tube section from a previous study (Liu *et al.* 2012a). Lee *et al*. (2016) used the finite element method to investigate the buckling behavior of steel girders considering the summer thermal loads. Among the parameters that were investigated are the width and thickness of the flange. Deng *et al.* (2015) used the finite element method to analyze the effect of temperature variation on the vibration response of cable-beam structures. They showed that the thickness of the beam is a key parameter.

Wang *et al.* (2010) carried out experimental temperature measurements on I-shape and tube steel specimens. The temperature records were continued for five months from April to September. The measurements revealed that a non-uniform temperature difference of 10°C was recorded during the test period. Liu *et al.* (2012b) conducted experimental temperature measurements on an H-shape steel segment under the direct effect of solar radiation. Using the experimental measurements, they verified a finite element model to investigate some solar parameters and the orientation of the longitudinal axis on the temperatures of the section. Liu *et al.* (2012a) conducted an experimental investigation using a steel tube segment. Temperature sensors were used to measure the steel surface temperatures and air temperature. They used a finite element thermal model of the steel tube to investigate some solar parameters in addition to the size and orientation of the beam. They found that the section diameter was an effective parameter, while its thickness was not. Chen *et al*. (2018) conducted an experimental and numerical study on three different-shape steel sections. The investigated steel sections were rectangular, I-shaped and circular. They concluded that the member size and the coating of its surface in addition to solar radiation intensity are the most dominant factors on temperature distributions along the section.

Several studies are available on the impact of solar radiation and air temperature variation on thermal response and temperature distributions in concrete members, while previous works by the author focused on the influence of environmental thermal loads on box and I-concrete girders in addition to composite girders. On the other hand, the previous literature review shows that the effect of temperature variation on steel members and steel structures has been investigated by some previous studies. However, and according to the best of the author's knowledge, no previous study has dealt in details with the influence of the geometrical parameters of steel beams on their thermal response under the variation of solar radiation and air temperature. Therefore, this research was directed aiming to evaluate the influence of the size and configurations of steel beams on the temperature distributions induced due to exposure to environmental thermal loads during the construction period. For this purpose, an experimental steel beam was instrumented with many temperature and other sensors and a finite element parametric study was conducted.

2. Experimental work

Fig. 2(a) shows the experimental steel beam segment, while Fig. 2(b) shows its geometrical dimensions of and the location of the temperature sensors. The beam segment was fabricated of 8 mm thickness steel plates. The depth of the experimental beam is 500 mm, while the width of the top and bottom flanges is 200 mm. The length of the segment is 500 mm and as shown in the figure it is simply supported on two wooden blocks. The beam was instrumented with seven type-T thermocouples installed along the central section of the beam, hence, 250 mm from the beam edges.

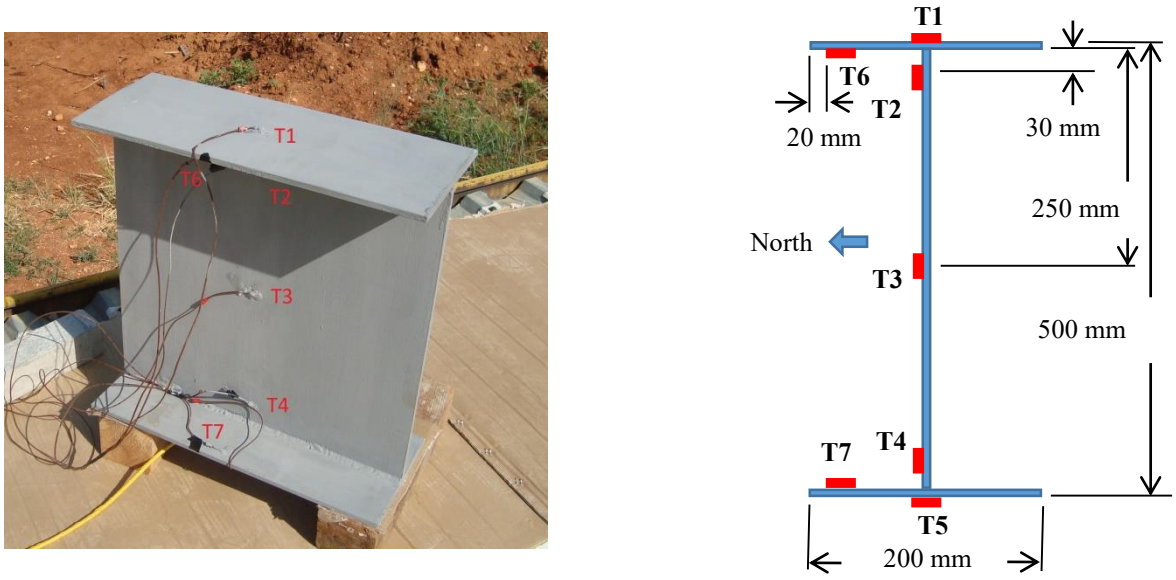

(a) (b)

Fig. 2 The experimental steel beam and the sensors

To ensure that the thermocouples are not affected by the direct solar radiation, the thermocouples were covered with a layer of epoxy after attachment to the steel plate.

Five thermocouples were distributed over the depth of the beam to evaluate the vertical temperature distributions, while two thermocouples were attached to the interior surfaces of the top and bottom flanges. The first thermocouple was installed at the top surface of the top flange (T1), while a thermocouple was installed at the lower surface of the bottom flange (T5). Three thermocouples (T2, T3 and T4) were installed on the northern surface of the web. The thermocouples T2, T3 and T4 were installed at distance of 30 mm from the top surface, at the central depth of the beam and at 30 mm from the bottom surface of the beam, respectively, as shown in Figs. 2(a) and 2(b). On the other hand, thermocouple T6 was installed at 20 mm from the northern edge of the bottom surface of top flange, while T7 was installed at the same distance from the edge of the top surface of the bottom flange.

Three sensors were used to measure the ambient thermal loads that affect the thermal budget of the beam. The air temperature was measured using an air temperature probe, which is protected from the direct solar radiation using a special solar shield. Three-cub anemometer was used to measure the speed of the wind in the site, while a pyranometer was the sensor that measures the solar radiation intensity. All readings from the thermocouples and the other sensors were recorded each 30 minutes and collected using a CR1000 data logger and AM16/32 multiplexers. The records of the three environmental sensors were collected directly through the data logger, while the multiplexer was used to acquire the records of the seven thermocouples. The data acquisition system and the three sensors of the environmental thermal loads were provided by Campbell Scientific. The software of the data logger allows to collect the experimental records automatically and are simply saved as excel sheets along the required period of time.

3. Experimental results

The experimental measurements from the thermocouples and the three environmental sensors were collected continuously along three weeks, from early morning of 5-June-2015 to midnight of 25-June-2015. In this section, the experimental air temperature, solar radiation and wind speed records are presented for this period. The temperature measurements from the thermocouples are also presented along the test perion. In addition, derived temperature measurements, such as hourly maximum temperature differences and temperature difference distributions, are also presented and discussed. The temperature difference along the vertical axis of the beam is calculated by subtracting the minimum temperature there from the temperature of the other thermocouples. Thus, the temperature of the thermocouple that showed the minimum temperature along the vertical axis is set to zero. In this case, the temperature difference is postive and represent the distribution along the heating hours (day hours). On the other hand, during the cooling hours (night hours), the opposite stands and the distribution becomes negative with the maximum temperature set to zero.

3.1 Air temperature, solar radiation and wind speed

The records of air temperature are essencial to evaluate two of the important thermal loads that affect the bridge temperature variations. Both the convection and the long wave re-radiation are dependent of air temperature. Fig. 3(a) shows the air temperature variation during the 21 days

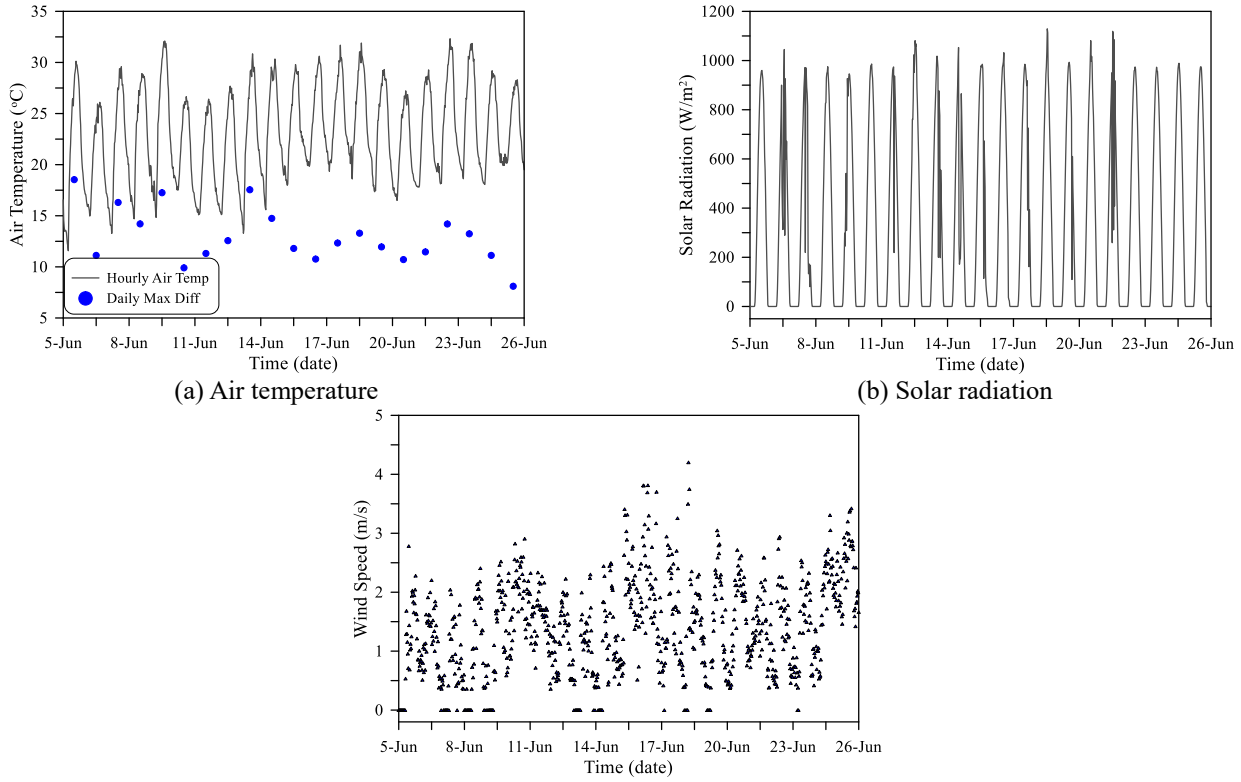

(a) Air temperature

(b) Solar radiation

(c) Wind speed

Fig. 3 Environmental thermal loads during the test period

from 5-June to 25-June. As shown in the figure the daily maximum temperature during this period was in the range of 26.1 to 32.3ºC, while the daily minimum temperature ranged from 11.6 to 19.9ºC. The daily maximum temperature of the bridge is affected by the daily maximum air temperature. However, to evaluate the daily maximum temperature difference, the daily temperature difference between the daily maximum and minimum air temperatures is much likely required. During the 21 days, the highest recorded daily temperature difference was 18.5ºC, while the lowest was only 8.1ºC as shown in Fig. 3(a).

Solar radiation is the main source of heat on the earth surface. In addition to the solar thermal load, the air is warmed during the day due to solar radiation and cooled during the absence of sunrays along the night hours. Thus, solar radiation controls the whole heating and cooling processes of the beam surfaces. Therefore, presenting solar radiation variation is required to investigate the temperature variation of the beam. Fig. 3(b) shows the variation of the solar radiation intensity in W/m^2 during the test period. As shown in the figure, the sky was mostly sunny during the test period, however, the flucuation of solar radiation during some days refers to the presense of a fluctauted cloud cover during these days. The recorded daily maximum hourly solar radiation during the test period was in the range of 946 and 1129 W/m^2. As wind speed is an effective factor on the convection cooling, it is presented in Fig. 3(c). The daily maximum wind speed during the period under study ranged from 2.0 to 4.2 m/s.

3.2 Thermocouple temperatures

Three thermocouples were selected to present the beam temperature variation with time along the 21 days. These three thermocouples are the top surface (T1), the mid-depth (T3), and the bottom surface (T5) thermocouples as shown in Figs. 4(a)-4(c), respectively.

Comparing the three figures, the behavior of the daily temperature variation of the three thermocouples is almost the same, which highly follows that of air temperature. It is obvious in the figures that the top surface thermocouple exhibited the highest daily maximum temperatures, while the mid-depth thermocouple (T3) showed the lowest ones. On the other hand, no significant variation is noticed between the daily minimum temperature records of the three thermocouples. Thus, the daily temperature variation is the highest at thermocouple T1 and the lowest at the thermocouple T3. This result is better visualized in Fig. 5, which compares the daily variation of the normalized temperatures of T1, T2, and T3 with the normalized air temperature during the 24 hours of 14-June-2015. The normalization was conducted by dividing the temperature of each thermocouple at each time step of the 24 hours by the maximum temperature recorded for this thermocouple in this day. The same procedure was followed for the normalized air temperature shown in Fig. 5. Hence increasing the difference between the daily maximum and minimum temperatures is shown in Fig. 5 as lower normalized temperatures during the cooling hours. The figure shows that the daily temperature variation is higher

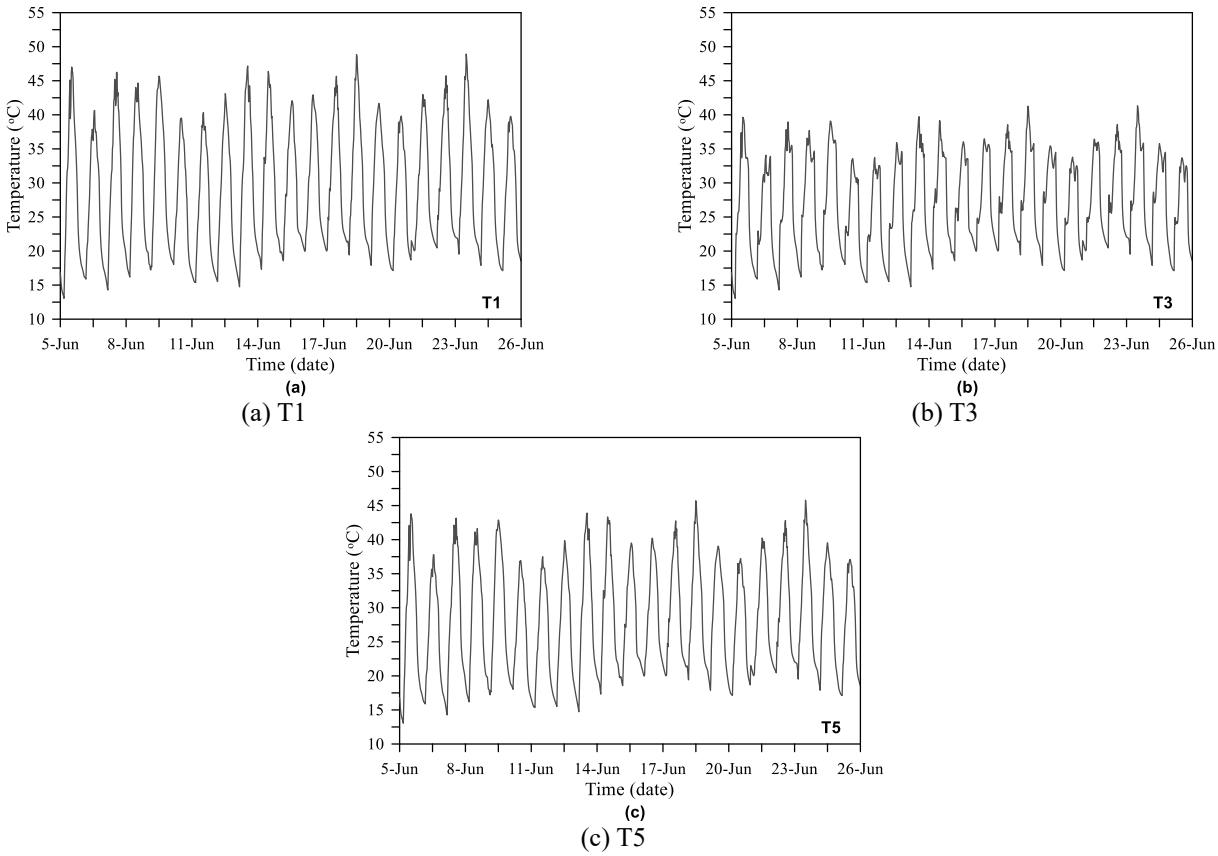

(a) T1 (b) T3

(c) T5

Fig. 4 Temperature variation of selected thermocouples during the test period

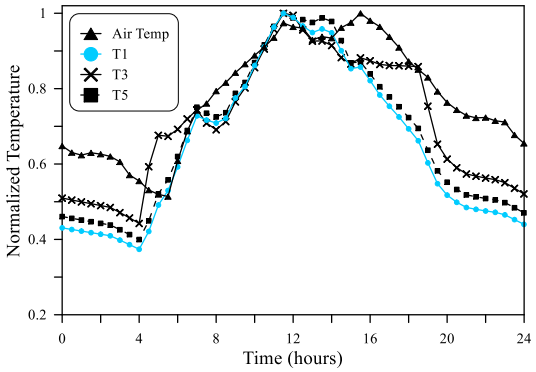

Fig. 5 Normalized thermocouples temperatures VS normalized air temperature in 14-June-2015

for thermocouple T1 than the other two thermocouples, while all thermocouples seem to show daily temperature variation that is significantly affected by that of air temperature. During the whole test period, the maximum recorded temperatures at thermocouples T1, T3 and T5 were 48.9, 41.3 and 45.8°C, while the recorded minimum temperatures for all thermocouples were almost equal and slightly higher than 13°C. This means that the maximum recorded temperature difference along the test period was approximately 38.9°C at T1, while it was approximately 28.3 and 32.7°C at T3 and T5, respectively.

Fig. 6 shows the hourly maximum temperatures and temperature differences of the beam during the test period together with air temperatures. It is clear that both the maximum temperature and the temperature difference distributions follow the hourly and daily variations of air temperature. However, close examination of the daily tips (noon and early afternoon hours) of these variations clarify that there are some minor differences between the three temperatures. These differences are attributed to the direct effect of solar radiation on the variation of the maximum temperatures and temperature differences of the beam. The daily maximum temperature difference along the vertical centerline of the beam ranged from 6.03 to 8.15°C.

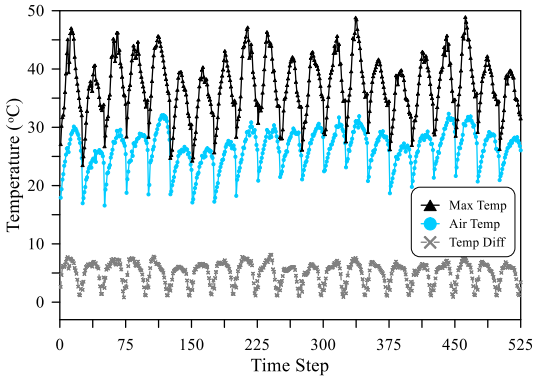

Fig. 6 Temperature differences and the beam's maximum temperature VS air temperature during the test period

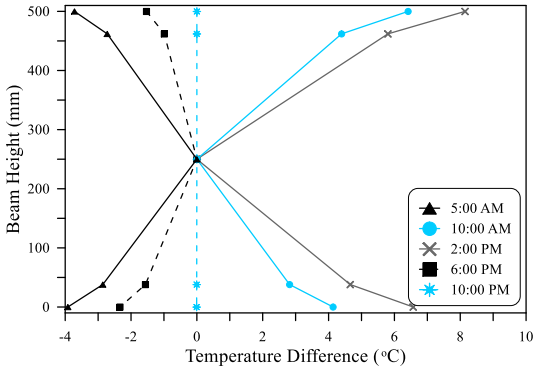

Fig. 7 Vertical temperature difference distributions at different time steps in 14-June-2015

3.3 Vertical temperature differences

As discussed in the previous section, the temperatures of the top and bottom surfaces are higher than along the web during the day hours, this variation in temperature leads to the vertical temperature differences shown in Fig. 7 at 10:00 AM and 2:00 PM. When the temperature of the top surface is greater than the temperature of the web, a positive temperature difference occurs, which increases during the sunshine hours to reach maximum 2 to 3 hours after midday. As shown in Fig. 7, the positive temperature difference at 2:00 PM is apparently higher than at 10:00 AM. Few hours before sunset, the temperature difference tends to decrease reaching almost zero temperature before midnight. The temperature distribution at 10:00 PM shows that the continuous convection cooling and the surface long-wave radiation have cooled down the flanges temperature so that the temperature of all parts became almost equal to air temperature. As the cooling process continues, the temperature of the flanges (top and bottom surfaces) becomes lower than the web, which is cooled slower. As a result, negative vertical temperature difference distribution forms with lower temperatures at the top and bottom surfaces than the web as shown in Fig. 7 at 5:00 AM before sunrise. It should be noted that after sunrise and before sunset the sunshine is directly subjected to the web vertical surfaces due to the low inclination angles of sunrays, while the flanges receive only minimal amount of solar radiation. Thus, the temperature of web at these times becomes higher than the temperature of flanges leading to the negative temperature difference distribution shown in Fig. 7 at 6:00 PM (before sunset).

4. Finite element thermal analysis

4.1 The thermal budget of the steel beam

The Fourier heat conduction equation (Eq. (1)) controls the process of the heat conduction and temperature (T) variation at any time (t) through the beam mass, which is dependent of the thermal conductivity coefficient (k), the specific heat (C_p), and the density of the steel (ρ). The boundary conditions of Eq. (1) are represented by Eq. (2), in which n_x, n_y, and n_z are the direction cosines of the vectors normal to the beam surfaces and q is the sum of the thermal loads on the boundaries of the beam (Ghali *et al.* 2012).

$$k\left(\frac{\partial^2 T}{\partial x^2}+\frac{\partial^2 T}{\partial y^2}+\frac{\partial^2 T}{\partial z^2}\right)=\rho C_p\frac{\partial T}{\partial t} \tag{1}$$

$$k\frac{\partial T}{\partial x}n_x+k\frac{\partial T}{\partial y}n_y+k\frac{\partial T}{\partial z}n_z+q=0 \tag{2}$$

Fig. 1 summarizes all types of ambient thermal loads on the steel beam, which are mainly due to three key loads; the solar radiation, air temperature, and wind speed. As shown in the figure, the radiation from the sun can mainly reach the surface by two direct beam radiation and diffuse

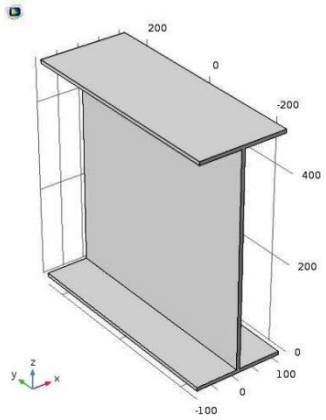

(a) Geometry of the FE model

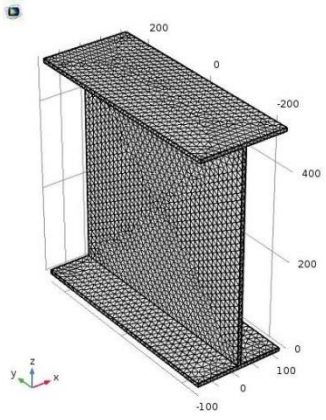

(b) Mesh of the FE model

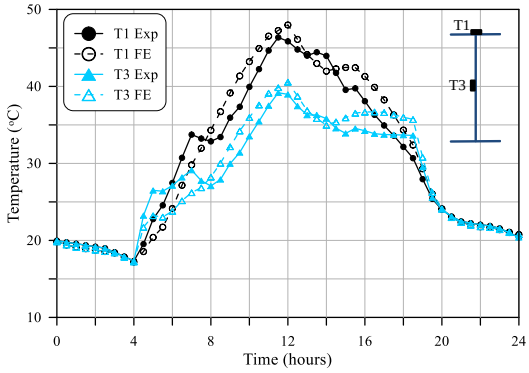

(c) Temperatures at T1 and T3

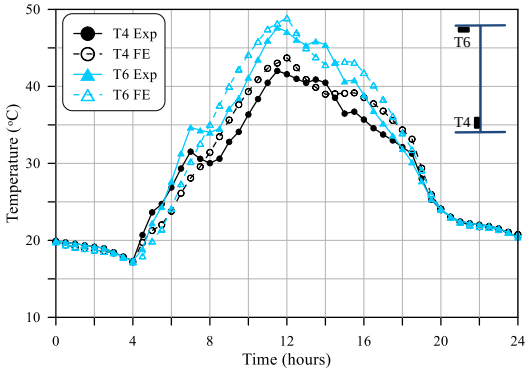

(d) Temperatures at T4 and T6

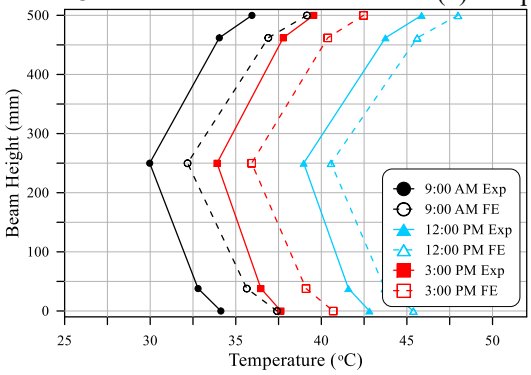

(e) Temperatures distribution along the beam heigh

Fig. 8 Verification of the FE thermal analysis

radiation, the summation of which composes the total solar radiation reaches the beam surface (I_s). The beam absorbs some a part of (I_s) depending on its absorptivity coefficient (α). The solar radiation may also reach the surfaces of the girder as reflected radiation from the ground (I_r). The amount of the reflected radiation depends on the ground reflectivity coefficient or albedo (a) and on the tilt angle of the beam surface with respect to the ground (δ) as shown in Eq. (3). The heat absorbed by the surface due to I_s and I_r is termed as (q_s), and is given in Eq. (4).

$$I_r = aI_s\left(\frac{1-cos\delta}{2}\right) \tag{3}$$

$$q_s = \alpha(I_s + I_r) \tag{4}$$

The beam absorbs some of the received radiation depending on its surface absorptivity (α), and reflects the rest amount of radiation. Some of the surface re-radiation reaches the other surfaces of the beam that have mutual vision and vice versa, which is called as surface-to-surface or mutual radiation (q_m) as shown in Fig. 1. The long wave re-radiation (q_{re}) from the beam surfaces is controlled by the difference between the temperatures of the beam surface (T_s) and the ambient air (T_a) around the beam. It also depends on the ability of the beam to diffuse solar radiation, which is controlled by the surface diffusivity coefficient of the steel beam (ϵ). Eq. (5) describes the long-wave re-radiation, in which (β) is a constant equals $5.67 \times 10^{-8}\, W/m^2K^4$. Another direct heat exchange between the beam surface and the ambient air, which is considered is the

main cooling load, is the convection heat transfer (q_c). The convection heat transfer is given in Eq. (6) and is controlled by the convection coefficient (h) (Lee 2012).

$$q_{re} = \epsilon\beta(T_s^4 - T_a^4) \quad (5)$$

$$q_c = h(T_s - T_a) \quad (6)$$

The summation of all of the above thermal loads, which is represented in Eq. (7), is the thermal boundary loads of the beam (q).

$$q = q_s + q_m + q_{re} + q_c \quad (7)$$

4.2 Finite element modeling and verification

The finite element analysis of the steel beam was conducted using COMSOL Multiphysics (2012). The boundary thermal loads described in the previous section and in Fig. 1 were all applied. The input air temperature, solar radiation and wind speed were those measured from the experimental data acquisition system. Fig. 8(a) shows the geometry of the conducted finite element analysis, while Fig. 8(b) shows the mesh of the analyzed beam. Fine tetrahedral elements were the main bone of the finite element model, while other surface and line elements were generated to apply the surface boundary conditions. These elements were found in previous researches to better simulate the mass and boundary conditions with high accuracy (Abid *et al*. 2014, Tayşi and Abid 2015, Abid *et al*. 2016b, Abid *et al*. 2017, Abid 2018). The finite element thermal model was verified with the experimental temperatures measured during the 24 hours of 14-June-2015. The initial time was setup at midnight where the temperature is approximately uniform through the steel girder. To eliminate the influence of this assumption, the analysis was started 48 hours before the target day (14-June).

To assure that that the finite element thermal analysis is accurate enough, the outputs of this analysis should be verified with experimental records. For this purpose, the finite element temperatures at the locations of the experimental thermocouples were compared with those obtained from the data acquisition system during the 24 hours of 14-June. Fig. 8(c) compares between the experimentally recorded and the finite element obtained temperatures at thermocouples T1 and T3 during the 24 hours of 14-June at time intervals of 30 minutes. Similarly, Fig. 8(d) shows the experimental and finite element temperatures for the same time period at thermocouples T4 and T6. The figures show that the variation of the finite element temperatures with time could capture the real variation of temperature at these locations with adequate accuracy, which refers to the good simulation of the boundary thermal loads and their time-dependent variation. On the other hand, the error between the recorded temperatures from the experimental beam (Exp) and their corresponding temperatures obtained from the finite element thermal analysis (FE) were low enough to support the adequacy of the model to capture the thermal behavior of the beam. The average absolute error, which is the sum of the absolute differences between the measured and predicted temperatures of the 48 time steps divided by 48, was in the range of 1.31 to 1.53°C for the seven thermocouples. The maximum absolute error between the measured and predicted temperatures during the 48 time steps of 14-June was generally less than 4°C, except at time step at thermocouple T6 where a maximum absolute error of 4.4°C was recorded

To further verify the accuracy of the conducted finite element analysis, the distributions of temperature differences along the vertical axis of the beam were compared between the measured and predicted temperatures as shown in Fig. 8(e). These comparisons are presented in the figure at midday (12:00 PM), three hours before middy (9:00 AM) and three hours after midday (3:00 PM). Such times where chosen because the maximum expected temperature variations occur during this time period as solar radiation is highly effective on the thermal budget of the beam. It is shown that the finite element predicted vertical temperature distributions exhibit the same variation as their corresponding experimentally measured ones at the three time steps. The average absolute error and the maximum absolute error of the vertical temperature difference were 2.9 and 3.3°C, respectively at 9:00 AM, while they were 2.0 and 2.6°C at 12:00 PM and 2.6 and 3.0°C at 3:00 PM, respectively.

5. Geometrical parametric studies

5.1 Study description

During the construction of steel structures, the steel beams are left open to environment conditions for long periods. These conditions include the thermal loads from the variation of air temperature and solar radiation, which are time-dependent. The aim of this section is to evaluate the influence of the daily variation of air temperature and solar radiation on steel beams during the construction period. For this purpose a parametric study was directed using the verified finite element thermal model from the previous section. The air temperature and solar radiation records of 14-June-2015 were used in this study, however, the wind speed was set to zero to maximize the thermal effects. The experimental temperature records of this study showed that the highest positive temperature differences within the beam section occur one to two hours after midday, while the maximum negative temperature differences occur before sunrise. Therefore and to optimize the discussion in this section, the temperatures are compared within these two periods, hence, 5:00 AM and 2:00 PM were chosen for comparison purposes.

The parametric study is subdivided into five studies to investigate the effect of five geometrical parameters. These are the height (depth) of the section, the width of the flange, the thickness of the flange and web, the overall size of the beam and the shape of the beam. To conduct a more realistic study, different sections from the AISC Steel Construction Manual were selected to satisfy the aims of the study. The sections are mainly W-shape. However, HP-

Table 1 The selected AISC steel sections

Shape	Weight Kg/m	Area (A) mm^2	Height (H) mm	Web Thickness (t_w) mm	Flange Width (B_f) mm	Flange Thickness (t_f) mm	Study
W44×335	498.5336	63548.26	1117.6	26.162	403.86	44.958	S
W40×593	882.47888	112257.8	1092.2	45.466	424.18	82.042	t_f
W40×397	590.79952	75483.72	1041.4	30.988	408.94	55.88	t_f
W40×331	492.58096	62903.1	1036.32	30.988	309.88	54.102	S
W40×277	412.22032	52516.02	1008.38	21.082	401.32	40.132	w_f
W40×235	349.7176	44516.04	1008.38	21.082	302.26	40.132	H , w_f
W40×215	319.9544	40903.14	990.6	16.51	401.32	30.988	t_f
W36×330	491.0928	62580.52	957.58	25.908	421.64	46.99	S
W30×326	485.14016	61806.33	822.96	28.956	391.16	52.07	S
W27×336	500.02176	63806.32	762	32.004	370.84	57.912	S
W24×370	550.6192	70322.44	711.2	38.608	347.98	69.088	t_f
W24×335	498.5336	63483.74	698.5	35.052	342.9	62.992	S
W24×229	340.78864	43354.75	660.4	24.384	332.74	43.942	t_f
W24×104	154.76864	19741.9	612.14	12.7	325.12	19.05	t_f , w_f
W24×84	125.00544	15935.45	612.14	11.938	229.108	19.558	w_f
W21×201	299.12016	38193.47	584.2	23.114	320.04	41.402	H
W12×336	500.02176	63741.81	426.72	45.212	340.36	75.184	S
W12×305	453.8888	57806.34	414.02	41.402	335.28	68.834	t_f
W12×190	282.7504	35999.93	365.76	26.924	322.58	44.196	t_f
W12×170	252.9872	32258	355.6	24.384	320.04	39.624	H
W12×79	117.56464	14967.71	314.96	11.938	307.34	18.669	t_f
W12×58	86.31328	10967.72	309.88	9.144	254	16.256	w_f
W12×50	74.408	9419.336	309.88	9.398	205.232	16.256	w_f , Sh
S12×50	74.408	9419.336	304.8	17.4498	139.192	16.7386	Sh
HP12×53	78.87248	9999.98	299.72	11.049	304.8	8.509	Sh

shape and S-shape beams were also analyzed for comparison purposes. Totally, 25 AISC steel beam sections were used in this parametric study. Table 1 lists the selected AISC sections and their geometrical properties.

The results of the parametric studies are presented in terms of vertical temperature distributions at the times of maximum and minimum vertical temperature differences. These distributions were selected because based on which the vertical temperature difference distributions and hence the self-equilibrating stresses are form. To unify the terms of study for all sections, the distributions were presented using a vertical grid of points, at which the temperatures were drawn. This grid composes of five equally spaced points along the thickness of each flange, while the web was divided by nine points into ten equal parts. Thus, a total of 19 points were used to draw the vertical temperature distributions used in the parametric study.

5.2 Effect of the beam size

To evaluate the overall effect of the beam size on the thermal behavior of the steel beams, the cross-sectional area or the unit weight of the section was chosen to be similar for all sections. Thus, different size sections with approximately the same cross-sectional area (unit weight) were chosen to evaluate the effect of the overall size of the beam. The selected beams are shown in Table 1, where the letter (S) in the study field means that this section is used for this study. Seven sections were selected with a unit weight of approximately 490 kg/m or a cross-sectional area of approximately 63000 mm^2. The actual unit weights of the selected sections were in the range of approximately 485 to 500 kg/m, while their cross-sectional areas were in the range of approximately 61800 to 63800 mm^2 as shown in Table 1.

Fig. 9 shows that as discussed previously during the early morning hours (before sunrise), the vertical temperatures distribution is negative with lower temperatures at the top and bottom surfaces (Fig. 9(a)), while it becomes positive with hotter top and bottom surfaces during the hot-temperature hours as shown in Fig. 9(b). Fig. 9(a) shows that larger beams exhibit wider vertical temperature distributions as the difference between the surface and mid-web temperatures are larger than those

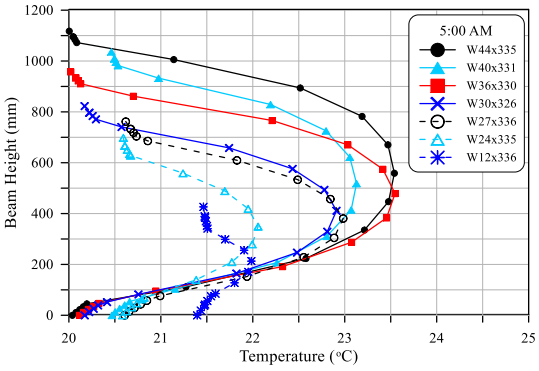

(a) At 5:00 AM

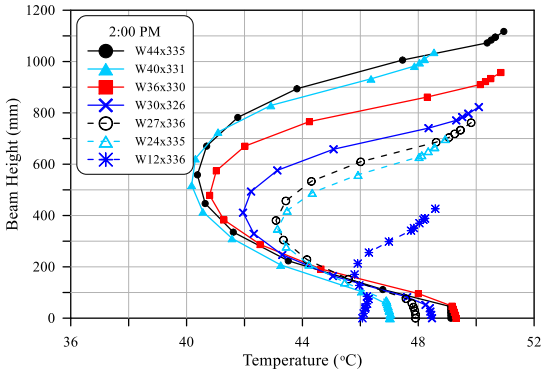

(b) At 2:00 PM

Fig. 9 Effect of overall size of the beam on temperature distribution

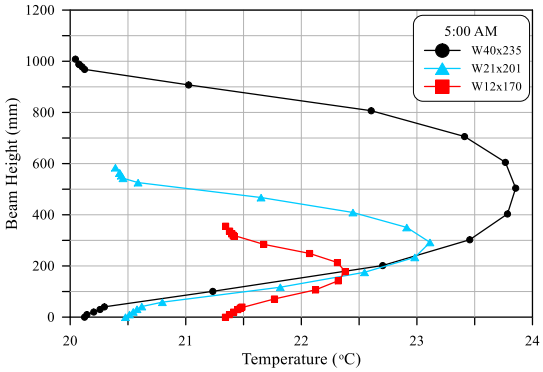

(a) At 5:00 AM

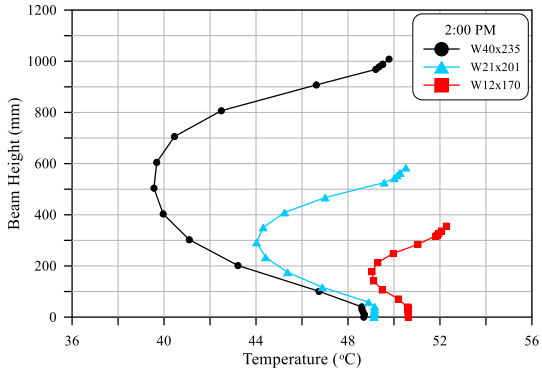

(b) At 2:00 PM

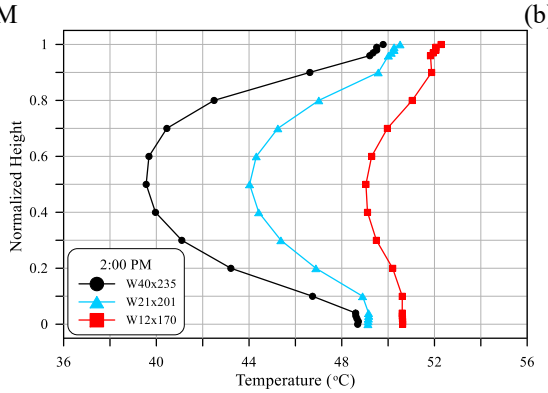

(c) At 2:00 PM considering normalized beam height

Fig. 10 Effect of beam depth on temperature distribution

of smaller sections. At 5:00 AM, the top surface temperature of W12×336 was 21.5°C, while the maximum temperature along the web was 22°C. On the other hand, for W44×335 and W27×336, the temperatures of the top surface at 5:00 AM were 20 and 20.6°C, respectively, while their corresponding temperatures at the mid-height of the web were 23.5 and 23°C, respectively. For the seven sections, W44×335, W40×331, W36×330, W30×326, W27×336, W24×335 and W12×336, the vertical temperature differences at 5:00 AM were 3.5, 2.7, 3.5, 2.7, 2.4, 1.5 and 0.6°C, respectively.

Similarly, Fig. 9(b) shows the vertical temperature distributions of the seven sections and confirms that the vertical temperature distributions of the large sections are wider with greater temperature differences than small sections. At 2:00 PM, the vertical positive temperature differences of W44×335, W40×331, W36×330, W30×326, W27×336, W24×335 and W12×336 were 10.6, 8.4, 10.0, 8.1, 6.7, 5.8 and 2.8°C, respectively. These results lead to one conclusion is that for the same cross-sectional area and unit weight, larger sections suffer higher vertical temperature differences, both for the positive and negative distribution cases. However, without studying the effect of each particular geometrical parameter, it is difficult to specify the most effective parameters on this result.

5.3 Effect of beam height

To investigate the effect of the beam height (H) on the thermal behavior of the steel beams, the other geometrical parameters should be kept constant. However, such a choice is not available when standard sections are selected as these sections have specific geometries. Therefore, the choice was made to keep the flange width and flange thickness constant as possible. The problem is that there are wide variety between the dimensions of the large sections (W40) and small sections (W12). The best three beams to conduct this study were found to be W40×235, W21×201 and W12×170. The three beams have a flange thickness of approximately 40 mm and a flange width of approximately 320 mm. However, for the heavy sections (W40), selecting a beam with flange width close to 320 mm, would increase the flange thickness by approximately 1.5 times the chosen thickness of the other two sections. Although the chosen section (W40×235) has a width of 302 mm, it is believed that the effect of such width difference is minimal as the depth of this beam exceeds 1000 mm.

Fig. 10 shows that deeper beams have much wider temperature distributions, which means that they suffered higher temperature differences. Fig. 10(a) shows that at 5:00 AM, the temperature of the top surfaces of W40×235, W21×201 and W12×170 sections were 20, 20.4 and 21.4 ^{o}C, respectively, while the corresponding temperatures at the center of the webs were 23.9, 23.1 and 22.4^{o}C, respectively. Thus, the vertical negative temperature differences at 5:00 AM of the W40×235, W21×201 and W12×170 sections that have heights of approximately 1008 , 584 and 356 mm were 3.8, 2.7 and 1.0^{o}C, respectively. On the other hand, at 2:00 PM, the shorter sections were in general hotter than deeper sections. However, their vertical positive temperature differences were smaller than those of deeper sections as shown in Fig. 10(b). The positive vertical temperature differences of the W40×235, W21×201 and W12×170 sections at 2:00 PM were 10.2, 6.5 and 3.2^{o}C, respectively. For better comparison, Fig. 10(c) shows the same distributions at 2:00 PM considering normalized height. The figure shows that although the temperatures of the shorter sections are higher than of deeper sections, their temperature differences are lower. Based on this comparison, it can be concluded that the increase of the depth of the section, considering similar flange width and thickness, leads to an increase in the vertical temperature differences, both during the negative and positive difference periods.

5.4 Effect of flange and web thicknesses

As for the other geometrical parameters, to study the effect of the flange thickness (t_f), the other geometrical parameters should not be variable. However, this is also not completely possible as the sections are already chosen from available standard sections. To evaluate the effect of the flange thickness, the size of the beams and the flange width should not be variables. For this reason, this parametric study was conducted on three groups of sections with different sizes of W40, W24 and W12 to eliminate the effect of the beam size. From each of the three groups, three beams were selected with approximately similar flange widths to reduce the effect of this parameter on this study. The selected beams from the first group are W40×593, W40×397 and W40×215. These beams have flange widths ranging from 401 to 424 mm, while their flange thicknesses are approximately 82, 56 and 31 mm, respectively. However, as sections become heavier, not only the flange thickness increases, but the web thickness also increases simultaneously. For the same sections, the web thicknesses are approximately 45, 31 and 17 mm, respectively. The second group composes of the standard beam W24×370, W24×229 and W24×104 with flange width of approximately 325 mm to approximately 348 mm, while their flange thicknesses are approximately 69, 44 and 19 mm, respectively, and their web thicknesses are approximately 39, 24 and 13 mm, respectively. Finally, the third group in this parametric study includes three W12 sections with flange widths ranging from approximately 307 mm to approximately 335 mm. These sections are W12×305, W12×190 and W12×79 and their flange thicknesses are approximately 69, 44 and 19 mm, respectively, while their web thicknesses are also variable as shown in Table 1.

Fig. 11 shows that the top and bottom surfaces are hotter at 5:00 AM for sections with thicker flanges, while these surfaces are colder at 2:00 PM as the thickness of the flange increase. The temperature of the top surface of sections W40×593, W40×397 and W40×215 with flange thicknesses of 82, 56 and 31 mm were 21.4, 20.8 and 19.8 ^{o}C, respectively at 5:00 AM, while they were 47.4, 50.2 and 52, respectively at 2:00 PM. Similar results are also shown in Fig. 12 for W24 sections and in Fig.13 for W12 sections. An explanation of these results is that thicker flanges need more heating energy to worm during the hot hours than thinner flanges. Thus, to reach the same temperature, thicker flanges require longer periods than thinner ones. Consequently, and as the same heating energy is applier for the same period, thicker flanges are colder during the hot hours. The opposite stands during the cooling hours (night hours). Thicker flanges save higher energies because of their size during the hot hours, hence, these sections loose temperature slower than thinner sections during the cooling hours and as a result, their temperatures are higher during the night and early morning hours.

Fig. 11 shows that as the thickness of the flanges and webs increase the vertical temperature difference decrease both at 5:00 AM and at 2:00 PM. The vertical temperature differences of sections W40×593, W40×397 and W40×215 at 5:00 AM were 1.8, 3.1 and 5.0 ^{o}C, respectively, while the vertical temperature differences at 2:00 PM were 7.5, 9.3, 12.8 ^{o}C, respectively. Similarly, for sections W24×370, W24×229 and W24×104 with flange thicknesses of 69, 44 and 19 mm, the vertical temperature difference sequences at 5:00 AM and 2:00 PM were 1.9, 2.8 and 4.5 ^{o}C and 5.3, 6.9 and 9.7 ^{o}C, respectively. Similar sequence of increase in vertical temperature differences with the decrease of the flange and web thicknesses can be noticed for W12 sections in Fig. 13. As a result of the previous discussion, it can be drawn that for sections having similar depths and flange

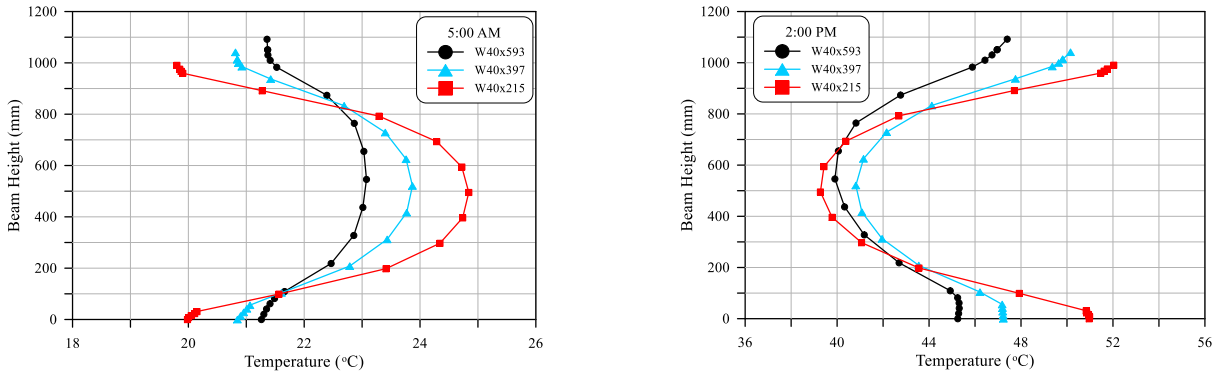

(a) At 5:00 AM (b) At 2:00 PM

Fig. 11 Effect of flange thickness (W40 sections) on temperature distribution

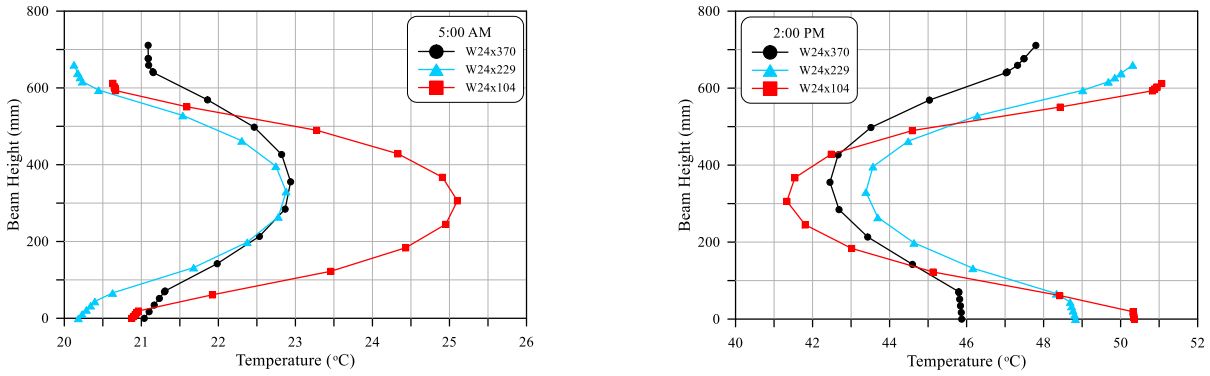

(a) At 5:00 AM (b) At 2:00 PM

Fig. 12 Effect of flange thickness (W24 sections) on temperature distribution

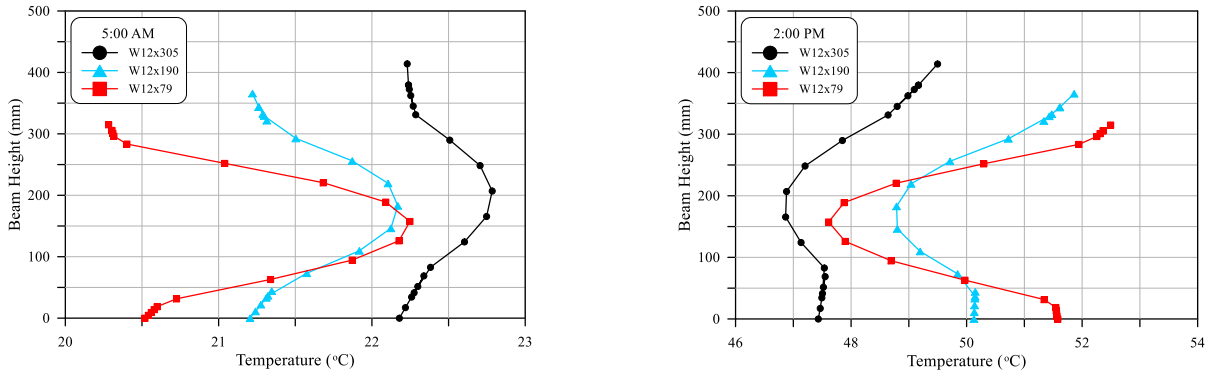

(a) At 5:00 AM (b) At 2:00 PM

Fig. 13 Effect of flange thickness (W12 sections) on temperature distribution

widths, the flange and web thicknesses significantly affect the vertical temperature difference values both at the times of negative and positive differences, where the temperature differences increase as the thickness of the flanges and webs decrease.

5.5 Effect of flange width

Similar to the previous section, the effect of the flange width (w_f) was investigated using three groups of specimens, each includes beams with different flange widths but with the same flange thickness. Each group in this study includes only two beams as it was difficult to satisfy the above terms considering more beams for each group. The first group includes W40×277 and W40×235, where both have a flange thickness of approximately 40 mm whereas their flange widths are 401 and 302 mm, respectively, as listed in Table 1. Similarly, the second group includes W24×104 and W24×84 with a fixed flange thickness of approximately 19 mm and widths of 325 and 229 mm, respectively. The third group includes W12×58 and W12×50 with fixed flange thickness of approximately

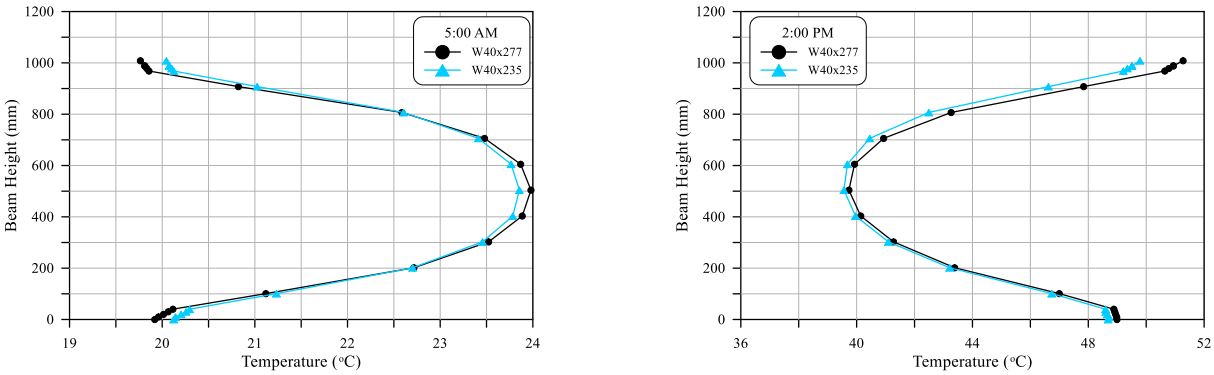

(a) At 5:00 AM (b) At 2:00 PM

Fig. 14 Effect of flange width (W40 sections) on temperature distribution

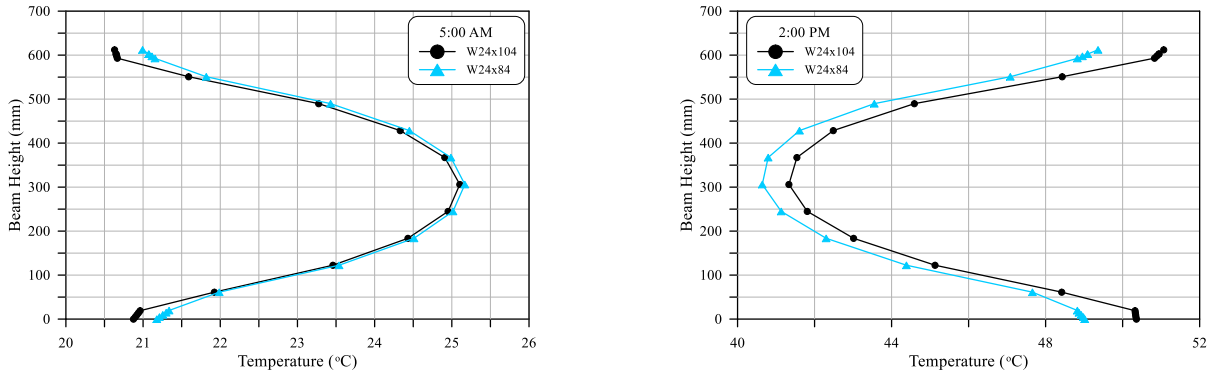

(a) At 5:00 AM (b) At 2:00 PM

Fig. 15 Effect of flange width (W24 sections) on temperature distribution

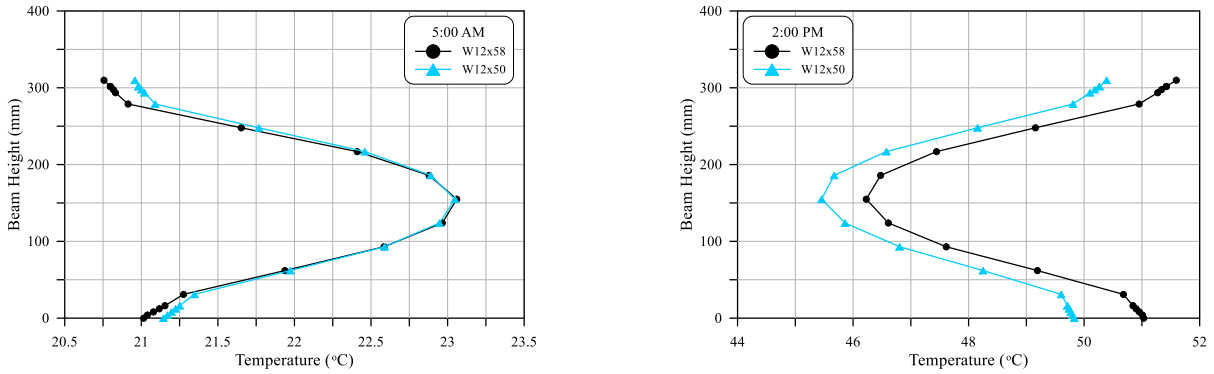

(a) At 5:00 AM (b) At 2:00 PM

Fig. 16 Effect of flange width (W12 sections) on temperature distribution

16 mm and two different flange widths of approximately 254 and 205 mm, respectively.

Fig. 14 shows that the variation between the temperature distributions of W40×277 and W40×235 are small both at 5:00 AM and 2:00 PM. The two sections have almost the same depths and same flange thicknesses but with different flange widths of 401 and 302 mm, respectively. The section with wider flange showed slightly higher temperature difference than that having smaller width flange. This difference is clearer at 2:00 PM than at 5:00 AM, but still small. The vertical temperature differences of sections W40×277 and W40×235 were 4.2 and 3.8°C, respectively at 5:00 AM, while they were 11.5 and 10.2°C, respectively at 2:00 PM. Similar results were obtained for the W24 sections and the W12 sections as shown in Figs. 15 and 16, respectively. The vertical temperature differences of sections W24×104 and W24×84 were 4.5 and 4.2°C at 5:00 AM and 9.7 and 8.7°C at 2:00 PM, respectively. Similarly, for W12×58 and W12×50, the vertical temperature differences were 2.3 and 2.1°C at 5:00 AM and 5.4 and 4.9 °C at 2:00 PM, respectively. This means that within the studied range of flange width variation, the particular effect

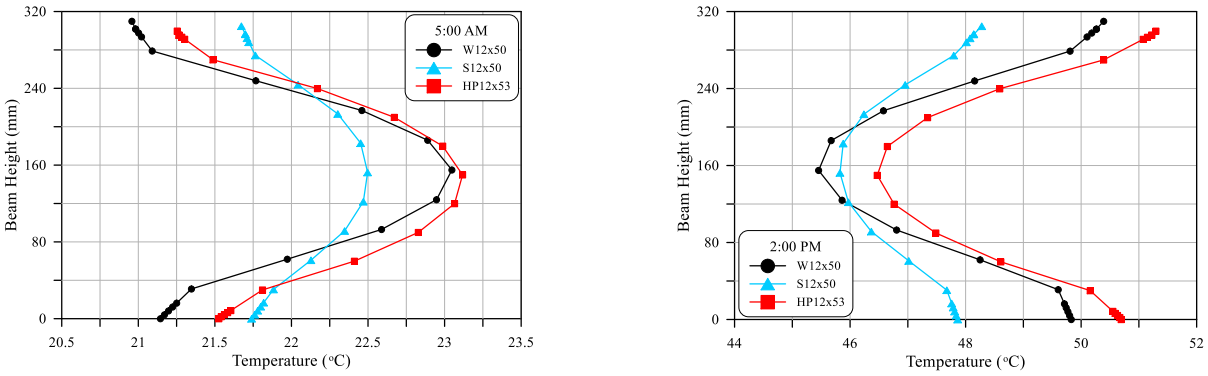

(a) At 5:00 AM (b) At 2:00 PM

Fig. 17 Effect of beam shape on temperature distribution

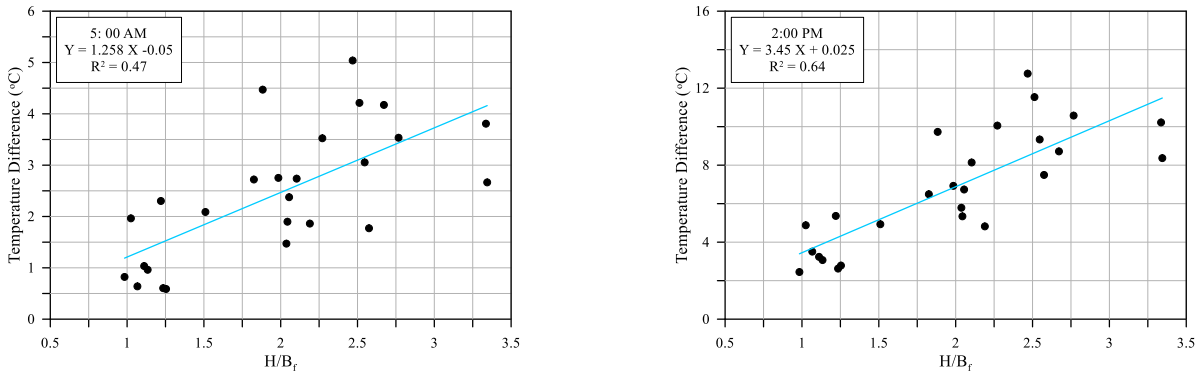

(a) At 5:00 AM (b) At 2:00 PM

Fig. 18 Beam depth/flange width-temperature difference relationship for the selected sections

of flange width on the vertical temperature distributions and differences can be considered as minimal.

5.6 Effect of section shape

Three beam shapes were selected to evaluate the effect of beam shape on the thermal behavior under environmental thermal loads. These are the W-shape, S-shape, and HP-shape. Three sections of same size and have approximately the same cross-sectional area and unit weight were selected for this purpose. The selected beam sections are W12×50, S12×50 and HP12×53 with cross-sectional areas of approximately 9400 to 10000 mm^2 and unit weights of approximately 74 to 79 kg/m. The three sections have almost the same height of approximately 300 to 310 mm, while the flange width is different for the three sections. The flange thickness is approximately equal for the W and S-shapes, which is approximately twice that of the HP-shape.

It is shown in Fig. 17 that the W and HP sections almost have similar wide temperature distribution and similar temperature difference values both at 5:00 AM and 2:00 PM, while the S section shows lower vertical temperature differences at the two times than the other two sections. The temperature differences at 5:00 AM for the W12×50, S12×50 and HP12×53 were 2.1, 0.8 and 1.9°C, respectively. On the other hand, the temperature differences of the three sections at 2:00 PM were 4.9, 2.5, and 4.8°C, respectively. The high temperature differences of the HP shape can be attributed to its wide and small thickness flanges, where flange width is almost the same as the beam depth. In contrary, the small temperature differences of the S-shape can attributed to its thick and small width flanges. Although, the flange thickness of the W-shape section is almost the same as that of the S-shape, its web thickness is smaller than those of both S and HP-shapes. Moreover, the flange width is approximately 1.5 times that of the S-shape. As HP sections are mostly used as compression members, it can be concluded that for the same depth and the same cross-sectional area (unit weight), W-shapes exhibit larger vertical temperature differences than S-shape beams.

5.7 Ratio geometrical parameters

In this section, the maximum negative and positive temperature differences of the studied sections are drawn against some geometrical parameters that control the flexural and shear design of steel sections. The studied parameters are represented as ratios of the above investigated section parameters including beam height (H), width of flange (B_f), thickness of flange (t_f) and thickness of web (t_w). The studied geometrical ratio parameters are H/B_f, H/t_w and B_f/t_f.

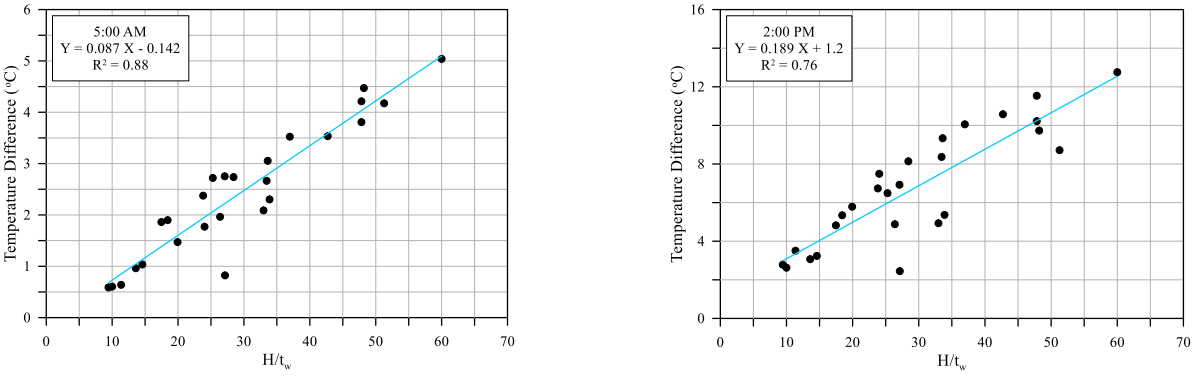

(a) At 5:00 AM (b) At 2:00 PM

Fig. 19 Beam depth/web thickness-temperature difference relationship for the selected sections

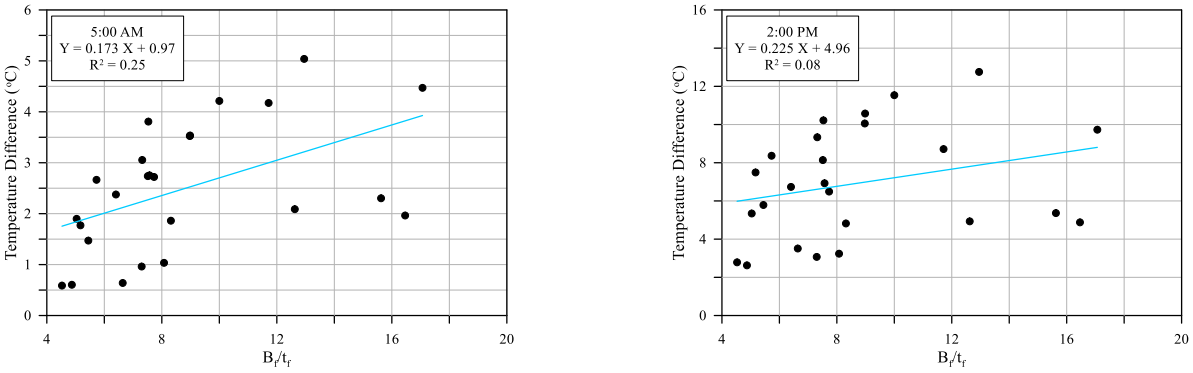

(a) At 5:00 AM (b) At 2:00 PM

Fig. 20 Flange width/flange thickness-temperature difference relationship for the selected sections

Fig. 18(a) shows the simple linear relationship between the predicted maximum temperature differences at 5:00 AM for the studied sections and their H/B_f values, while Fig. 18(b) shows this linear relationship at 2:00 PM. The figures show that the better relationship was obtained at 2:00 PM with higher coefficient of determination (R^2) of 0.64. Such moderate R^2 refers to a moderate dependency of the vertical temperature difference values on this parameter. This result is consistent with the results of the parametric studies discussed in the previous sections, where it was clarified that within the investigated range of dimensions, the depth of the beam has significant effect on the vertical temperature differences, while the effect of the flange width is minimal. Combining the two parameters in one parameter (H/B_f) would consequently leads to such result.

Fig. 19 shows the linear relationship between H/t_w and the maximum vertical temperature difference. In the previously discussed parametric studies, it was disclosed that the depth of the beam and the thickness of the sections are the most influential geometrical parameters on the vertical temperature difference. The relationships presented in Figs. 19(a) and 19(b) confirm these results. The figures show that good relationships with moderately high coefficient of determinations were obtained when H/t_w is considered. The coefficient of determination of this relationship ranges from 0.76 to 0.88. In contrary, Fig. 20 shows that poor relationships were obtained between the parameter B_f/t_f and the vertical temperature difference, which reflects the low dependency of the temperature difference on this parameter.

6. Conclusions

This paper presents an experimental study on temperature variation of a steel beam under environmental thermal loads. Based on the experimental steel beam, a finite element thermal analysis was conducted and verified to evaluate the thermal behavior of different shapes and different sizes AISC steel sections. From the experimental beam and the finite element thermal analysis, the followings are the most important conclusions.

- During the 21 days, the highest recorded daily air temperature difference was 18.5°C, while the lowest was only 8.1°C. On the other hand, the daily maximum houlry solar radiation ranged from 946 to 1129 W/m^2. For these thermal loads the daily maximum temperature difference along the depth of the experimental steel beam (vertical temperature difference) was in the range of approximately 6.0 to 8.2 °C. The daily variation of the vertical temperature difference along the test period was found to be more dependent on that of air temperature than of solar radiation.

- The temperature records of the thermocouples installed at different locations on the surface of the experimental steel showed that the daily temperature variations of these thermocouples are more affected by the variation of air temperature than of solar radiation. Moreover, the daily maximum temperature variation was measured at the thermocouple of the top surface of the beam, which recorded the highest temperature, while the daily minimum temperature was almost the same at all thermocouples. During the 21-day test period, the maximum recorded temperature variations at thermocouples T1, T3, and T5 (top surface, mid-depth, bottom surface) were 38.9, 28.3, and 32.7ºC, respectively.
- From the finite element parametric study of the overall size of the beam using seven different-size beams that have approximately the same cross-sectional area and unit weight, it was found that the vertical temperature difference increases with the increase of the beam size. The maximum vertical temperature difference of the investigated largest section (W44×335) was 10.6ºC, while it was only 2.8ºC for the smallest section (W12×336).
- Using the AISC sections W40×235, W21×201 and W12×170 that have approximately the same flange thickness and flange width, the particular effect of the beam depth was investigated in the second geometrical parametric study. It was found that deeper sections suffer higher vertical temperature differences than shallower sections. The vertical temperature differences of W40×235, W21×201 and W12×170 at 2:00 PM were 10.2, 6.5 and 3.2 ºC, respectively.
- Other finite element geometrical parametric studies were conducted to evaluate the effect of the flange thickness and width. The results of these studies showed that, within the limits of the investigated dimensions, the thickness of the flange is more effective than the width of the flange on the thermal behavior of steel beams. It was also concluded that the depth of the section and the thickness of its members are the most influential parameters.
- Comparing three similar unit weight beams, it was found that S-shape beams exhibit lower vertical temperature differences than W-shape and HP-shape beams. The vertical temperature differences of S12×50, W12×50 and HP12×53 at 2:00 PM were 2.5, 4.9 and 4.8ºC, respectively.
- The results of the parametric studies also showed that the correlation between the vertical temperature difference and the ratio of the beam depth to web thickness (H/t_w) was better than that of the beam depth to flange width (H/B_f), while it was much better than that of flange width to flange thickness (B_f/t_f)

Acknowledgments

The experimental work described in this research was conducted in Gaziantep University/ Turkey. The author would gratefully express his gratitude to Prof. Dr. Mustafa Özakça and Assoc. Prof. Dr. Nildem Tayşi for their support.

References

Abid, S.R. (2018), "Three-dimensional finite element temperature gradient analysis in concrete bridge girders subjected to environmental thermal loads", *Cogent Eng.*, **5**(1), 1-15.

Abid, S.R., Mussa, F., Tayşi, N. and Özakça, M. (2018), "Experimental and finite element investigation of temperature distributions in concrete-encased steel girders", *Struct. Control Health Monit.*, **25**(1), 1-23. https://doi.org/10.1002/stc.2042.

Abid, S.R., Tayşi, N. and Özakça , M. (2014), "Three-dimensional thermal modeling of temperature variation in concrete box-girders using COMSOL",*Proceedings of the 2014 COMSOL conference in Cambridge*, Cambridge, UK.

Abid, S.R., Tayşi, N. and Özakça , M. (2016a), "Experimental analysis of temperature gradients in concrete box girders", *Constr. Build. Mater.*, **106**, 523-532. https://doi.org/10.1016/j.conbuildmat.2015.12.144.

Abid, S.R., Alrebeh, S., Tayşi, N. and Özakça, M. (2016b), "Finite element thermal analysis of deep box-girders", *Int. J. Civil Eng. Technol.*, **7**(1), 128-139.

Alinia, M.M. and Kashizadeh, S. (2006a), "Effect of flexibility of substructures upon thermal behaviour of spherical double layer space truss dome: Part I: Uniform thermal loading", *J. Constr. Steel Res.*, **62**(7), 359-368.

Alinia, M.M. and Kashizadeh, S. (2006b), "Effect of flexibility of substructures upon thermal behaviour of spherical double layer space truss domes. Part II: Gradient & partial loading", *J. Constr. Steel Res.*, **62**(7), 675-681. https://doi.org/10.1016/j.jcsr.2005.11.003.

Chen, D., Qian, H., Wang, H., Chen, Y., Fan, F. and Shen, S. (2018), "Experimental and numerical investigation on the non-uniform temperature distribution of thin-walled steel members under solar radiation", *Thin-Wall. Struct.*, **122**, 242-251. https://doi.org/10.1016/j.tws.2017.10.018.

COMSOL Multiphysics v 4.3. (2012), *COMSOL Multiphysics User's Guide*, Stockholm, Sweden.

Deng, H.Q., Li, T.J., Xue, B.J. and Wang, Z.W. (2015), "Analysis of thermally induced vibration of cable-beam structures", *Struct. Eng. Mech.*, **53**(3), 443-453. https://doi.org/10.12989/sem.2015.53.3.443.

Ghali, A., Favre, R. and Elbadry, M. (2002), *Concrete Structures: Stresses and Deformation*, 3rd Edition, London: E & FN Spon.

Giussani , F. (2009), "The effects of temperature variations on the long-term behaviour of composite steel-concrete beams", *Eng. Struct.*, **31**(10), 2392-2406. https://doi.org/10.1016/j.engstruct.2009.05.014.

Kim, S.H., Park, S.J., Wu, J. and Won, J.H. (2015), "Temperature variation in steel box girders of cable-stayed bridges during construction", *J. Constr. Steel Res.*, **112**, 80-92. https://doi.org/10.1016/j.jcsr.2015.04.016.

Kromanis, R. and Kripakaran, P. (2014), "Predicting thermal response of bridges using regression models derived from measurement histories", *Comput. Struct.*, **136**, 64-77. https://doi.org/10.1016/j.compstruc.2014.01.026.

Kulprapha , N. and Warnitchai , P. (2012), "Structural health monitoring of continuous prestressed concrete bridges using ambient thermal responses", *Eng. Struct.*, **40**, 20-38. https://doi.org/10.1016/j.engstruct.2012.02.001.

Lee, J., Jeong, Y. and Kim, W. (2016), "Buckling behavior of steel girder in integral abutment bridges under thermal loadings in summer season during deck replacement", *Int. J. Steel Struct.*, **16**(4), 1071-1082. https://doi.org/10.1007/s13296-016-0023-x.

Lee, J.H. (2012), "Investigation of extreme environmental conditions and design thermal gradients during construction for

prestressed concrete bridge girders", *J. Bridge Eng.*, **17**(3), 547-56. https://doi.org/10.1061/(ASCE)BE.1943-5592.0000277.

Liu, H., Chen, Z. and Zhou, T. (2012a), "Numerical and experimental investigation on the temperature distribution of steel tubes under solar radiation", *Struct. Eng..Mech.*, **43**(6), 725-737. https://doi.org/10.12989/sem.2012.43.6.725.

Liu, H., Chen, Z. and Zhou, T. (2012b), "Theoretical and experimental study on the temperature distribution of H-shaped steel members under solar radiation", *Appl. Therm. Eng.*, **37**, 329-335. https://doi.org/10.1016/j.applthermaleng.2011.11.045.

Liu, H., Chen, Z. and Zhou, T. (2013a), "Investigation on temperature distribution and thermal behavior of large span steel structures considering solar radiation", *Adv. Steel Constr.*, **9**(1), 41-58.

Liu, H., Chen, Z. and Zhou, T. (2013b), "Temperature distribution and structural behavior of box-sectional arch structures under solar radiation", *Adv. Steel Constr.*, **9**(4), 298-308.

Lucas, J.M., Berred, A. and Louis, A. (2003), "Thermal actions on a steel box girder bridge", *Structures and Buildings, ICE Proceedings*, **156**(SB2), 175-182.

Nandan, H. and Singh, M. (2014), "Effects of thermal environment on structural frequencies: Part 1-A simulation study", *Eng. Struct.*, **81**, 480-490. https://doi.org/10.1016/j.engstruct.2014.06.046.

Numan, H., Tayşi, N. and Özakça, M. (2016), "Experimental and finite element parametric investigations of the thermal behavior of CBGB", *Steel Compos. Struct.*, **20**(4), 813-832. https://doi.org/10.12989/scs.2016.20.4.813.

Song, Z., Xiao, J. and Shen, L. (2012), "On temperature gradients in high-performance concrete box girder under solar radiation", *Adv. Struct. Eng.*, **15**(3), 399-415. https://doi.org/10.1260/1369-4332.15.3.399.

Tayşi, N. and Abid, S.R. (2015), "Temperature distributions and variations in concrete box-girder bridges: experimental and finite element parametric studies", *Adv. Struct. Eng.*, **18**(4), 469-486. https://doi.org/10.1260/1369-4332.18.4.469.

Wang, Y., Shi, Y. and Lin, C. (2010), "Experimental study on the temperature of steel members in sunshine", *J. Build. Struct.*, **31**, 140-147.

Zhao, Z., Liu, H. and Chen, Z. (2017), "Thermal behavior of large-span reticulated domes covered by ETFE membrane roofs under solar radiation", *Thin-Wall. Struct.*, **115**, 1-11. https://doi.org/10.1016/j.tws.2017.01.025.

CC